ISSN 0021-3640, JETP Letters, 2024, Vol. 120, No. 7, pp. 531–539. © Pleiades Publishing, Ltd., 2024.
Russian Text © The Author(s), 2024, published in Pis'ma v Zhurnal Eksperimental'noi i Teoreticheskoi Fiziki, 2024, Vol. 120, No. 7, pp. 550–559.

METHODS OF PHYSICAL RESEARCH

Synchronous Detection of Nonlinear Phenomena in Opto-Acoustic Vibrations Induced in a Nanofilm by a Femtosecond Laser Pulse

V. A. Khokhlov[a] **(ORCID: 0000-0001-9126-0243), S. A. Romashevskiy**[b] **(ORCID: 0000-0001-6061-6702), S. I. Ashitkov**[b] **(ORCID: 0000-0003-3655-4585), and N. A. Inogamov**[a,b,c,]* **(ORCID: 0000-0002-7703-4415)**
[a] *Landau Institute for Theoretical Physics, Russian Academy of Sciences, Chernogolovka, Moscow region, 142432 Russia*
[b] *Dukhov All-Russia Research Institute of Automatics, Moscow, 127055 Russia*
[c] *Joint Institute for High Temperatures, Russian Academy of Sciences, Moscow, 125412 Russia*
**e-mail: nailinogamov@gmail.com*

Received July 16, 2024; revised August 27, 2024; accepted August 28, 2024

Studies of the laser-induced ultrafast processes in thin films are of significant importance for the development of microelectronics. These processes include the heating of an electron subsystem, relaxation and transport of the absorbed energy, and generation and propagation of picosecond acoustic waves. In view of this circumstance, to study the dynamics of variation of the differential reflection coefficient $\Delta R(t)/R_0$ of a 73-nm-thick Ni film on a glass substrate, pump–probe measurements have been performed in this work with the synchronous detection of a $\Delta R(t)/R_0$ signal. High absorbed fluences up to 11 mJ/cm^2 have been reached by increasing the period of following $t_{\rm cool}$ of the sequence of heating (pump) pulses. An increase in $t_{\rm cool}$ makes it possible to better cool the film after heating. As a result, record temperatures $T_e \approx 3$ kK and $T_i \approx 1$ kK and stresses up to 7 GPa have been reached for the first time to the best of our knowledge. These high values have allowed the observation of nonlinear effects for the first time in experiments with synchronous detection.

DOI: 10.1134/S0021364024603208

1. INTRODUCTION

Contactless noninvasive optical methods for analysis of thermal and mechanical properties with the nanoscale spatial resolution and femto- and picosecond time resolution are necessary for the optimization of the characteristics of thin films on substrates. Such materials provide the foundation of the modern solar energetics (photovoltaics) and electronic industry (heterostructures, topological isolators, and devices based on them). The implementation of such precise measurements requires the application of femtosecond lasers and synchronous detection methods [1–6].

An important consequence of the superfast heating of a material by femtosecond laser pulses is the generation of picosecond acoustic pulses (or coherent acoustic phonons) in the gigahertz and terahertz frequency ranges [7, 8]. Laser-induced acoustic pulses can be used, e.g., to detect the presence of hidden interfaces and structures through optically opaque materials (metals) with micron lateral and nanoscale lateral and nanoscale depth resolutions [9, 10]. To study optically transparent media using acoustic pulses, the time-domain Brillouin scattering method [11, 12] is used to obtain information on the acousto-optical properties of a studied material and on the presence of structural inhomogeneities with a nanoscale spatial resolution [13, 14].

The synchronous detection (SD) method allows one to identify a desired signal with a low amplitude at a certain frequency against the broadband noise background with a high amplitude. According to this method, the time variation of the differential reflection, $\Delta R(t)/R_0$, or transmission, $\Delta T(t)/T_0$, coefficient for the probe laser pulse is determined. Variations of the coefficients R and T are due to internal transient processes in an irradiated target, which are induced by the action of a pump pulse. The description of processes inside the target based on SD is similar in sense to that based on the velocity interferometer system for any reflector (VISAR) method [15–17], but at the picosecond scale rather than at nano- and microseconds. Thus, SD is applicable to the analysis of picosecond acoustics.

The significance of this work is that we have succeeded to apply the highly accurate SD method at increased fluences $F_{\rm abs}$ absorbed by the target, i.e., at much higher temperatures and pressures compared to those reached in the reported works with this widely used method. A weak heating by means of femtosecond laser pulses and the relaxation of the energy in thin nickel films were studied using SD in order to reveal the dynamics of ultrafast demagnetization [18], see also studies [6, 19] concerning opto-magneto-acoustic and magnetoplasmonic phenomena. experimental SD studies of fundamental laws of the interaction between the electron and phonon subsystems, as well as heat transport at nanoscales [3, 20, 21], were carried out only at low overheating of the electron subsystem.

The dynamics of the optical response using SD was studied in [22, 23] at high fluences F_{abs}, which were reached due to an increase in the time interval t_{cool} between heating laser pulses for the target after heating to return to the state at room temperature. However, studies reported in [22–24] were focused on the determination of the parameter of interaction α between the electron and phonon subsystems and the thermal conductivity κ in gold under the two-temperature (2T) conditions.

In this work, we consider opto-acoustical phenomena at high fluences F_{abs}. Gold studied in [23, 24] is inappropriate for the analysis of these phenomena because the interaction parameter α of gold is low and the thermal diffusivity $\chi_{2T} = \kappa_{2T}/c_e$, where c_e is the specific heat of the electron subsystem, is high under the 2T conditions [25]. In metals, the 2T values χ_{2T} can be two orders of magnitude higher than the one-temperature (1T, $T_e \approx T_i$) values $\chi_{1T} = \kappa_{1T}/c \sim 0.2–1$ cm^2/s [25], where c is the 1T specific heat. For crystals with one atom per unit cell, $c \approx 3nk_{\text{B}}$ according to the Dulong–Petit law. Electrons are strongly degenerate, and their contribution to the specific heat is much smaller than $3nk_{\text{B}}$ at relatively low electron temperatures T_e up to ~1 eV, whereas the Fermi energies of metals are ~10 eV. These circumstances are simply explained in [25]. Correspondingly, the 2T state in gold is very long (its duration is t_{eq}) and the heating depth in the 2T stage is very large: $d_T \approx 2\sqrt{\chi_{2T} t_{\text{eq}}} \sim$ 150–200 nm. The thermal wave during the 2T stage leaves the skin layer at the supersonic velocity. The acoustic stage follows after the end of the 2T stage and, correspondingly, after the end of the supersonic propagation of heat.

In this work, we study a nickel nanofilm on a glass substrate. The film is bounded by the interface with air from one side (it is the front edge) and by the nickel–glass interface from the other side. The interaction parameter α in nickel is larger than that in gold, the duration of the 2T stage t_{eq} is small, and the thermal diffusivity χ_{2T} and the heating depth d_T are smaller than the respective parameters in gold. The acoustic stage begins earlier than in gold and its beginning is sharper; therefore, this stage is clearly observed using SD [26]. The thickness of the heating layer d_T in nickel is slightly larger than the thickness of the skin layer $\delta_{\text{sk}} = 13$ and 12 nm for the first (793 nm) and second (396 nm) harmonics, respectively [27].

As known, after the end of the supersonic 2T stage (quasihomogeneous propagation of the absorbed energy deeper through the electron subsystem in almost immobile material), the pressure profile decays into two waves according to d'Alembert's principle. One of these waves (compression wave) immediately propagates deeper into the film. The other wave is reflected from the front edge (which is mechanically free), changes the sign of the amplitude, and propagates as a rarefaction wave following the first wave. As a result, the combination of the compression and rarefaction waves propagates into the film [28, 29]; it is called the z profile or zigzag wave according to its shape. In the linear acoustic approximation, a sharp jump exists between the compression and rarefaction waves. According to the experimental and numerical results presented below, the steepness of the jump decreases gradually due to nonlinear effects. This steepness in the linear case is always infinite.

2. EXPERIMENT

The source of radiation was a Ti:sapphire femtosecond subterawatt laser system (Legend, Coherent) with the regenerative amplification of chirped pulses. The system generated 60-fs 793-nm pulses with a repetition frequency of 1 kHz. A sample was a polycrystalline Ni film, which had the thickness $d_{\text{f}} = 73 \pm 2$ nm and a surface roughness of 6 nm, deposited on a 150-μm-thick borosilicate substrate by magnetron sputtering in an argon atmosphere at a pressure of 0.05 Torr.

The time dynamics of the differential reflection coefficient

$$\Delta R(t)/R_0, \tag{1}$$

where $\Delta R(t) = R(t) - R_0$, $R(t)$ and R_0 are the reflection coefficient induced in the studied sample by the *pump* pulse and the initial coefficient, respectively, was recorded using the *probe* pulse in the pump–probe scheme with SD [26, 30].

The pump pulse after the transformation into the second harmonic in a BBO crystal had a duration of $t_{\text{pump}} = 150$ fs and a wavelength of $\lambda_{\text{pump}} = 396$ nm. It was focused by a 200-mm lens at an angle of incidence of 45° into an elliptic spot with the $1/e$-level dimensions $d_x = 130$ μm and $d_y = 93$ μm. The variations of the coefficient given by Eq. (1) were detected in the center of the heating region using probe pulses. A probe pulse had a duration of $t_{\text{probe}} = 60$ fs and a wavelength of $\lambda_{\text{probe}} = 793$ nm. This pulse was focused by means of a 4X/0.10 micro-objective normally to the surface into a circular spot with the $1/e$-level diameter $d_x = d_y = 15$ μm.

An optical delay line was used to vary the time delay t_{delay} between the pump and probe pulses in the interval from –3 to 300 ps with the step from 30 fs in the early stage to 400 fs in later stages.

Small variations of the reflection coefficient specified by Eq. (1) with amplitudes of ~10^{-4}–10^{-2} were detected using SD, which allows one to measure weak periodic desired signals at a given frequency against noise using a synchronous amplifier [26].

Signals of the probe pulse, which was reflected from the sample and was incident on the sample, were detected by means of two photodiodes in the balance regime and were guided to the differential input of the synchrotron amplifier (SR830). In our variant of the SD method, the signal of Eq. (1) is measured at the repetition frequency 500 Hz of pump pulses (behind the mechanical interrupter), and the repetition frequency of pump pulses was 1 kHz.

The process of measurements was automated using software. The minimum detected changes in the signal of Eq. (1) in the applied scheme were ~5×10^{-5}.

The heating and measurement of the reflection coefficients given by Eq. (1) for the probe and pump pulses were performed from the front surface of the nickel film. Taking into account our measured value $R_{\rm pump} = 0.14$, the absorbed fluence $F_{\rm abs}$ of the pump pulse varied 0.906 to 10.87 mJ/cm^2. It is very important that it is the maximum possible fluence at the repetition frequency 500 Hz of pump pulses. In this case, all changes in the sample were irreversible. The methods of measuring (a) the fluence of the pump pulse incident on the target, (b) the reflection coefficient of the pump pulse, and (c) the size of the focusing spot were described in [24].

At higher $F_{\rm abs}$ values, reversibility is lost and the sample is destroyed. This destruction can be caused by two factors. First, mechanical loads at first tens of picosecond are quite high (see also [31]): field stresses up to 7 GPa in the film and ~1 GPa in glass for $F_{\rm abs} = 10.87$ mJ/cm^2. Second, the temperature is accumulated in long series of pump pulses. It is still unclear which of these two factors dominates in the destruction.

3. GRADUAL HEATING AT MULTIPLE REPETITIONS

According to the numerical simulation, in the time interval $t_{\rm cool} = 2$ ms between successive pump pulses, the film is cooled due to the heat removal. The radius of lateral heat flow over the film in the time between pump pulses is estimated at $r \sim 2\sqrt{\chi_{1T} t_{\rm cool}} = 440$ µm, where $\chi_{1T} \approx 0.2$ cm^2/s. The ratio of the heating and flow areas is about 20. The temperature of the film in the center of the heating spot after electron–phonon relaxation and the heating of the film over the thickness at times $t \sim 100$ ps increases by

$$\Delta T(F_{abs} = 10.87\ \mathrm{mJ/cm^2}) = 350\ \mathrm{K}. \qquad (2)$$

The glass layer having the thermal diffusivity $\chi_{\rm glass} \approx 5 \times 10^{-3}$ cm^2/s with the thickness $d_{\rm glass} > 60$ µm is heated under the film heating spot in the time $t_{\rm cool}$. The thickness $d_{\rm glass}$ is three orders of magnitude larger than the thickness of the film $d_{\rm f}$. The specific heats of the nickel and glass are 3.8×10^6 and 2.1×10^6 J/(K m^3), respectively. Due to the heating of glass in the time $t_{\rm cool}$, the increase in the temperature of the film decreases by a factor of 500. It is seen that the cooling of the film due to the heating of glass is stronger than cooling due to the heat flow over the film. The decrease in the temperature is determined by the ratio $20 \times 500 = 10^4$ of the initial and final (at the time $t_{\rm cool}$) volumes, which is the product of the area of the heat flow over the film and the penetration depth into the substrate. The thermal energy diffusing in space is concentrated in these volumes. The shape of this volume is elongated in area: the size of the heating spot on the film is 440 µm, while the glass heating depth is 60 µm, i.e., is smaller by a factor of 7.

Thus, the increase in the temperature of the film in the time $t_{\rm cool}$ immediately before the beginning of the next pump pulse decreases from the value given by Eq. (2) to

$$T^* = \Delta T(F_{abs} = 10.87\ \mathrm{mJ/cm^2})/10^4 = 0.04\ \mathrm{K}. \qquad (3)$$

Three scans were carried out in the experiment consecutively; i.e., the end of one scan is separated from the beginning of the next scan by the same time interval $t_{\rm cool}$. Measurements inside each of these scans were performed for all required values $t_{\rm delay}$. Approximately 175 pump pulses were spent for each $t_{\rm delay}$ value. Measurements for approximately 1100$t_{\rm delay}$ values were conducted in each scan. The total number of pump pulses in three scans was $N \approx 6 \times 10^5$ pulses. These measurements continued about 20 min.

The increase in the temperature of the target after M pump pulses is estimated in the form

$$\Delta T_{\rm fin} = \sqrt{N} T^*. \qquad (4)$$

The substitution of the above N value and T^* given by Eq. (3) under the assumption of the infinite size of the film and the infinitely thick glass layer into Eq. (4) gives 30 K. This estimate is based on the linearity of the linearity of the heat equation, the increase in the heating depth $\propto \sqrt{t}$, and the summation of contributions from successive pump pulses $\sum^{n=N} T^*/\sqrt{n}$.

The sizes and configuration of pump pulses should be taken into account in a real estimate because the duration of the experiment is long so that the heat induced by pump pulses spreads to significant distances from the focusing spot. For example, the radius of the heat spread over the film in 20 min is 30 cm. At $N = 6 \times 10^5$ and an absorbed energy of 1.2 µJ per pump pulse, the total energy transferred in a sample will be 0.7 J. Let the area of the film and the substrate be 1 cm^2 and the sample be thermally insulated. Then,

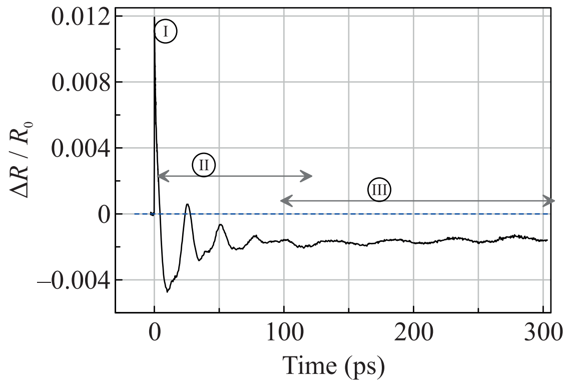

Fig. 1. (Color online) Time variation of the differential reflection coefficient given by Eq. (1) at the maximum value F_{abs} = 10.87 mJ/cm^2 at a frequency of 500 Hz demonstrating three characteristic stages: (I) the two-temperature stage lasting ~1 ps, (II) the stage of dominance of the acoustic echo in the nickel film, and (III) the Brillouin scattering of probe pulses on the acoustic wave propagating in the glass substrate.

the sample will be heated in three scans by 20 K at the uniform temperature distribution. Thus, the increase in the temperature given by Eq. (4) can be reduced by increasing the efficiency of the heat removal from the sample.

The dashed horizontal straight line in Fig. 1 marks the initial differential reflection coefficient of our target consisting of the film and substrate specified by Eq. (1). This coefficient for the 793-nm wave normally incident on a thick nickel sample is R_0 = 0.74. The reflection of the sample increases in the short 2T stage marked as I in Fig. 1. The correction given by Eq. (1) in this stage is positive. The increase in the reflection coefficient R is due to the redistribution of electrons between the Ni s- and d-bands $3d^8 4s^2$ or $3d^9 4s^1$ [32]. The large centrifugal potential of the 3d-band raises 3d electrons to the level of the fourth shell. The increase in the reflection coefficient in the 2T stage is quite typical of metals and the wavelength λ at which the reflection coefficient is low. The reflection of well-reflecting metals decreases in the 2T stage [24].

The reflection coefficient specified by Eq. (1) in the 1T stages indicated as II and III in Fig. 1 is primarily negative due to the heating of the film and a decrease in its density and, hence, in the plasma frequency. In this work, we analyze acoustic phenomena in stage II.

4. NONLINEAR LASER HYDRODYNAMICS

The features of strong nonlinear phenomena became clear already in the first works describing the interaction of ultrashort pulses with metals [33, 34]. They are, first, the formation of shock waves [35, 36], second, the delamination of films [37, 38], reverberation in the heated layer [39], and, third, the break of the condensed phase (nanospallation and cavitation) [29, 33, 39–43] due to strong tension. In [39, 41, 42], picosecond reverberations were observed in the solid phase at spallation or in a melt at the femtosecond laser ablation.

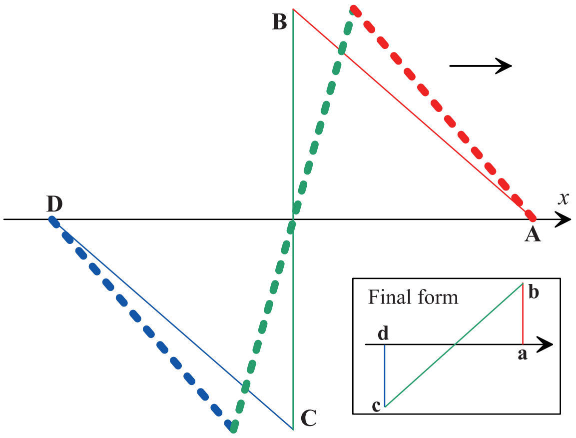

Fig. 2. (Color online) Instantaneous pressure profile in the acoustic wave ABCD, which is formed by femtosecond action and propagates to the right as indicated by the arrow. The irradiated front air/nickel interface remains on the left. In the linear approximation, the shape ABCD with the vertical jump BC remains unchanged. The nonlinearity-distorted profile is shown by dashed. The slope of the jump BC decreases gradually. The inset shows the shape abcd of the asymptotic wave consisting of two shock waves ab and cd and the family of characteristics bc.

Nanospallation destroys the target after a single pump pulse. For this reason, much weaker pump pulses are used to apply synchronous detection (multipulse action). In this case, the acoustic field is described in the linear approximation [1–4, 6].

The formation of a flow in the form of the “z wave” after the supersonic heating of a metal by the thermal electron wave was studied in [28, 29]. As mentioned above, the z profile ABCD in Fig. 2 is formed due to (a) the “instantaneous” (supersonic) formation of a pressure layer/profile with the thickness d_T in immobile (u = 0, this is important) material, (b) the decay of the supersonic-induced pressure profile according to d’Alembert’s principle at $p > 0$ and $u = 0$, and (c) the reflection from the interface with air.

The zigzag or z profile ABCD in Fig. 2 consists of the forward compression wave AB (red segment) $p > 0$ and the adjacent rarefaction wave CD (blue segment) $p < 0$. The sharp jump BC between these two components (green segment) is due to the reflection condition at the front edge. A change in the sign of the pressure and, thereby, the velocity $u = p/z$ is caused by the momentum conservation law, where z is the acoustic impedance of nickel. The momenta of absorbed and reflected photons can be neglected in the ratio of the velocity of hydrodynamic motion to the speed of light.

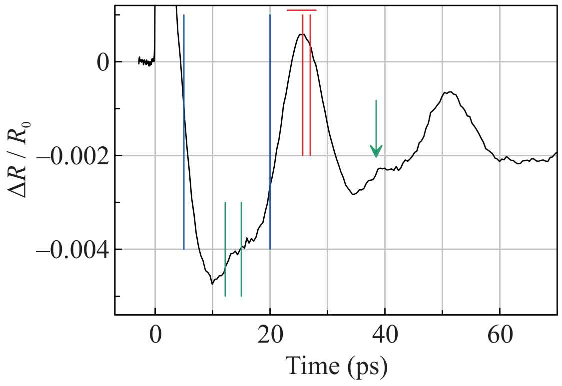

Fig. 3. (Color online) Fragment of the plot from Fig. 1 with two acoustic peaks. Two green vertical straight lines mark the first arrival of the rarefaction wave RW at the front edge fr, see Fig. 6. The green arrow marks the second arrival of the rarefaction wave RW at the front edge fr, see the main text.

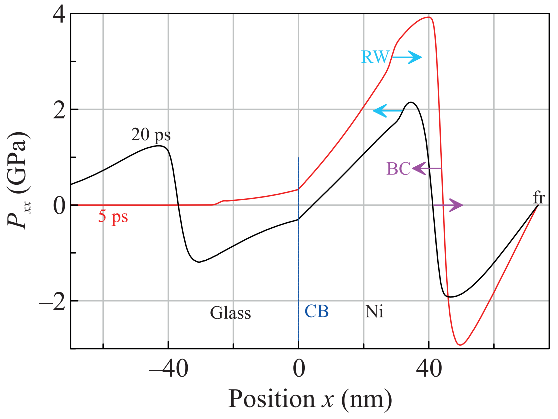

Fig. 4. (Color online) Acoustic field, which is the sum of the wave ABCD with the jump BC marked by violet arrows (see Fig. 2) and the rarefaction wave RW marked by blue arrows. The red and black lines are the first and second half-cycles each with a duration of ≈13 ps. In the first half-period, the singularities BC and RW travel from the front edge (fr) and the contact boundary CB, respectively. In the second half-period, the first reflections of these waves occur and the propagation directions are reversed. The shifts of the front edge fr and the contact boundary CB are less than 1 nm and are invisible in the presented scale. The steepness of the rarefaction wave RW is determined by the time of increasing pressure in nickel at the interface in the two-temperature stage.

The triangle shape in Fig. 2 is chosen for simplicity. The real shape is formed in the 2T stage and is close to Gaussian, which is the solution of the heat equation.

In the nonlinear case, the shape ABCD in Fig. 2 varies with time. At the points A and D, the wave propagates at the speed of sound c_0 because the material is immobile and the pressure at these points is zero. However, the situation is different at the crest (point B) and the dip (point C) of the wave. When the nonlinearity is taken into account in the first order of the perturbation theory, the velocity of the crest B is higher than c_0 by $\Delta v = (1/z + \partial c/\partial p)p$. Thus, the points B and C diverge with time at the velocity $2\Delta v$.

The first signature of the nonlinearity is a change in the slope of the family of characteristics BC (see Fig. 2). The nonlinear stage 1 ends with the wave breaking: the blue and red inclined segments in Fig. 2 are transformed to the shock jumps ab and cd shown in the inset of Fig. 2. The amplitude of the jumps ab and cd in the nonlinear stage 2 decrease as $1/\sqrt{t}$, see [44], due to the absorption of the characteristics of the family bc in shock waves ab and cd. The instantaneous amplitude of the jump is determined by the pressure p at the characteristic entering the jump at this time. The pressure p at the characteristic entering the jump at a longer time is lower. Correspondingly, the amplitude of the jump decreases with time. Our experiments at the highest fluences F_{abs} for the synchronous detection technique and numerical calculations revealed for the first time for this technique the development of optoacoustic processes in the nonlinear stage 1.

5. NUMERICAL SIMULATION AND COMPARISON WITH EXPERIMENTS

As in the VISAR method [15, 17], measurements of the reflection coefficient specified by Eq. (1) [1] concern the signal from the edge of the target, where transient processes proceed. Let us analyze processes inside the target using the 2T hydrodynamic simulation (2T-HD code [45]) in the isotropic elastic body approximation. Figure 3 presents in more detail stage II from Fig. 1. Vertical straight lines t = const mark the times at which processes inside the target were analyzed. Blue vertical straight lines refer to Fig. 4. Figure 4 clarifies the structure of the acoustic field inside the nickel film. Red vertical straight lines refer to Fig. 5 and are required to understand the physics of the formation of an acoustic burst. The length of the red horizontal bar over the first burst corresponds to the time of circulation of the characteristics BC through the skin layer (see Fig. 5). Green marks in Fig. 3 refer to the rarefaction wave RW.

The pump pulse generates an acoustic wave of the shape shown in Fig. 2 in the target. However, the z profile in Fig. 2 propagates in the infinite volume. In the case of our sufficiently thin 73-nm-thick film comparable in thickness with the "instantaneous" 2T heating layer d_T, the nickel–glass interface should be taken into account.

The heating thickness d_T in nickel at a wavelength of 396 nm used for the heating and at absorbed fluences $F_{\text{abs}} = 10.87$ and 0.906 mJ/cm^2 are $d_T \approx 30$ and 20 nm, respectively. The thickness d_T was determined from the half-height of the increase in the instantaneous profile of the electron temperature $T_e(x,t^*)$

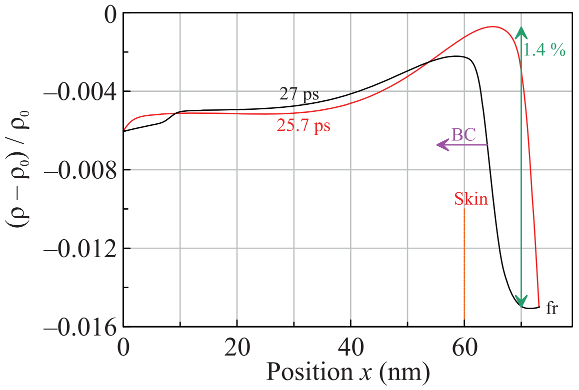

Fig. 5. (Color online) Reflection of the family of the characteristics BC of the wave ABCD (see Figs. 2 and 4) from the front edge fr at the times 25.7 and 27 ps marked by the red vertical straight lines in Fig. 3. The characteristics BC on the black profile are already reflected and move to the left. The forward and backward passage of the section BC through the 13-nm-thick skin layer takes 5 ps, which is shown in Fig. 3 as the horizontal red bar above the first acoustic burst (the first echo of the jump BC). The orange vertical straight line presents the thickness of the skin layer 13 nm.

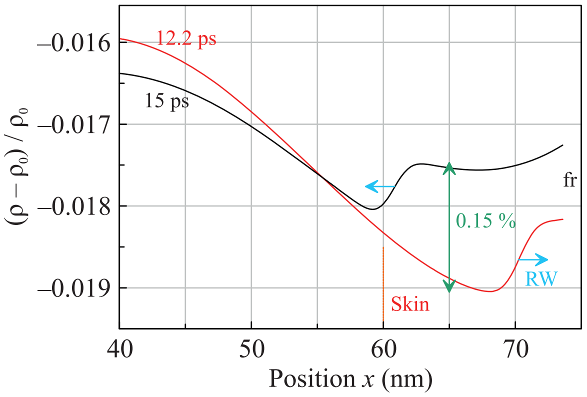

Fig. 6. (Color online) Reflection of the rarefaction wave RW (see Fig. 4) from the front edge fr at the times 12.2 and 15 ps marked by the green vertical straight lines in Fig. 3. The wave on the red (black) profile propagates to the right toward (to the left from) the front edge fr, respectively. The skin layer is marked by the script Skin.

compared to room temperature at the time t^* of reaching the maximum temperature T_e at the frontal (irradiated) surface obtained by the 2T hydrodynamic simulation.

The supersonic electron thermal wave rapidly (instantaneously for acoustic time scales) increases the pressure at the interface on the side of nickel. The acoustic impedance of glass is much smaller than that of nickel. Consequently, the rarefaction wave RW "instantaneously" begins to propagate from the interface into the nickel film due to the fast "switching-on" of the pressure in nickel at the interface.

Thus, two singularities of the acoustic field—the jump BC (see Figs. 2 and 4) and the rarefaction wave RW propagating from the interface (see Fig. 4)—propagate in the film (see Fig. 4). At acoustic time scales, they start at zero time into the film toward each other, one of them from the front edge and the other from the interface. Spikes on the dependences of the reflection coefficient specified by Eq. (1) in Figs. 1 and 3 are due to the arrival of these features at the skin layer for probe pulses, both pump and probe pulses are incident on the front side of the film, and the skin layer is adjacent to the front edge. The arrival of these features is responsible for the fast change in the density and, therefore, in the plasma frequency ω_p. The increase in the density of nickel in the skin layer increases the reflection coefficient given by Eq. (1).

Figure 5 demonstrates the range of the density variation in the skin layer at the reflection of the family of characteristics BC. We note that, although this range is sufficiently large (1.4%), a change in the density at the front edge itself is small (see Fig. 6). The hydrodynamic approach is applicable at scales of several interatomic layers. The dynamic boundary condition at the boundary in this boundary layer has the form $p_{xx}|_{\mathrm{fr}} = 0$. This condition is responsible for the smallness of the variation of $\rho|_{\mathrm{fr}}$ at the boundary. The density of nickel is lower than its initial density $\rho_0 = 8.907$ g/cm^3 because of the heating of the film. Therefore, the relative change in the density $(\rho - \rho_0)/\rho_0$ in Figs. 5 and 6 are negative.

6. RELATION BETWEEN HYDRODYNAMICS AND THE REFLECTION COEFFICIENT

The relative permittivity of nickel can be represented by the Drude formula

$$e_1 = 1 - \frac{\omega_p^2(1+\hat{\rho})}{\omega^2}, \quad e_2 = \frac{\omega_p^2(1+\hat{\rho})}{\omega^2(\omega\tau(1+\hat{\tau}))}. \tag{5}$$

Here, $\omega = 2.4 \times 10^{15}$ s^{-1} is the frequency of light oscillations at a wavelength of 793 nm, $\hat{\rho} = (\rho - \rho_0)/\rho_0$ and $\hat{\tau}$. are the dimensionless corrections to the density and collision time, respectively. The plasma frequency and the mean free time determined from the reference dielectric constant of nickel $e_1 = -18.8$ and $e_2 = 21.45$ for the wavelength $\lambda = 793$ nm under normal conditions are $\omega_p = 1.06 \times 10^{16}$ s^{-1} and $\tau = 0.39$ fs disregarding corrections to the deviation from these conditions.

The zeroth and first-order terms of the expansion of the reflection coefficient $R(\hat{\rho}, \hat{\tau})$ calculated in terms of the functions given by Eqs. (5) including corrections in small corrections much smaller than unity have the form

$$R = 0.74 + 0.11\hat{\rho} + 0.064\hat{\tau}. \tag{6}$$

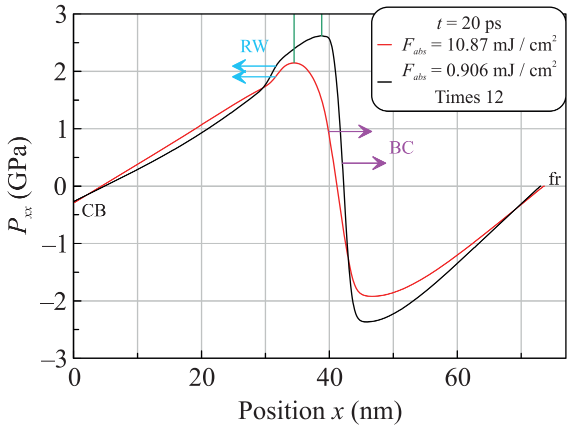

Fig. 7. (Color online) Illustration of the enhancement of a nonlinear phenomenon with increasing energy. Nonlinearity is manifested in the slope of the segment BC. It is seen that the maximum of ρ in the stronger wave moves to the right behind the maximum in the weaker wave due to the slope, as marked by the green vertical straight lines. This retardation leads to the shift of the maximum of the acoustic peak indicated by the Π mark in Fig. 8. The amplitude of the weak wave is increased by a factor of 1.2/0.1 = 12 in order to compare the weak and strong actions, see the main text.

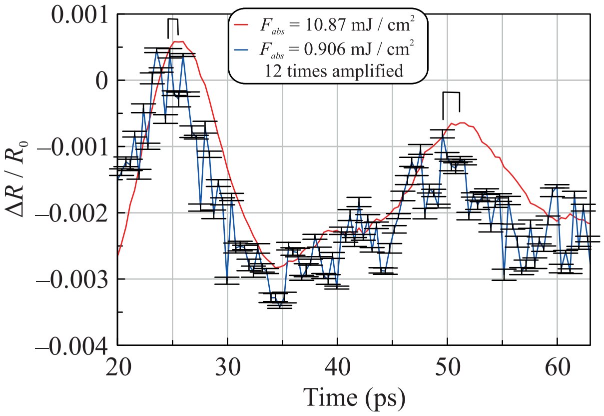

Fig. 8. (Color online) Manifestation of the nonlinearity in the detected delay of acoustic peaks under strong heating actions (see the red line) compared to weak actions (cf. the blue line with error bars). The corresponding delays for the first and second echoes are indicated by Π marks.

According to Eq. (6), the coefficient R increases with the density (and, hence, the plasma frequency ω_p) and the mean free time. This behavior is natural.

We take the correction $\hat{\rho} = 0.014$ and the average decrease in the relative density $\hat{\rho} = -0.008$ from Fig. 5 and $\hat{\tau} = 0$. Then, according to Eq. (6), the correction and the average decrease in the reflection coefficient specified by Eq. (1) are $0.11 \times 0.014/0.74 = 2.1 \times 10^{-3}$ and approximately -10^{-3}. These values are in satisfactory agreement with the dependence of the reflection coefficient given by Eq. (1) in Fig. 3.

The reflection coefficient specified by Eq. (1), which changes under the pump action, is called the transient thermoreflectance [1]. Indeed, the heating induced by the pump pulse generates the acoustic wave (see Section 4) and reduces the density of the film ($\hat{\rho} = -0.008$ and $\Delta R/R_0 \approx -0.001$ mentioned above). On the other hand, the appearance of the acoustic echo is due just to mechanical stresses.

7. NONLINEAR BROADENING OF CHARACTERISTICS BC

A change in the slope and, correspondingly, the broadening of the segment of characteristics BC are qualitatively described in Fig. 2. The situations with weak (the nonlinearity can be neglected at the considered times) and strong (the nonlinearity is significant) pump pulses with energies of 0.1 and 1.2 μJ, respectively, which differ by a factor of 12 and provide the absorbed fluences $F_{\text{abs}} = 0.906$ and 10.87 mJ/cm^2, respectively, are quantitatively compared in Fig. 7 at the time $t = 20$ ps belonging to the second half-period. The characteristics BC and the rarefaction wave RW are reflected once from boundaries. It is seen that the segment BC of the instantaneous profile of the stronger pulse has a larger slope. Correspondingly, the maximum of the density and frequency ω_p arrives the front edge fr later. This is manifested in the delay of the arrival of the peak maximum (see the Π mark in Fig. 8).

Figure 8 presents the experimentally detected nonlinear effect. To compare signals of the transient thermoreflectance given by Eq. (1) with different F_{abs} values, the weak signal was increased by a factor of 12, which is the higher-to-lower energy ratio. The error for the blue line shown in Fig. 8 is not increased by a factor of 12. The errors of the red line are the same and are not shown to avoid overloading the figure. Consequently, the weaker the action, the larger the relative error of the signal of the transient thermoreflectance given by Eq. (1).

8. CONCLUSIONS

Opto-acoustic phenomena have been analyzed in synchronous detection experiments with a thin nickel film and the two-temperature numerical simulation taking into account the elasticity of nickel. To the best of our knowledge, the process of approaching the front edge by the rarefaction wave has not yet been analyzed. The rarefaction wave is initiated in the short two-temperature stage at the nickel–glass interface.

The synchronous detection method has been applied at fluences extremely possible for it. The heat accumulation at multiple repetitions of pump pulses has been described. It has been discussed whether the limit of applicability of the method is determined by the gradual heating or by thermocycling-induced cracking or by their combination. The accuracy of the acquisition of the measurement statistics for the coefficient given by Eq. (1) is determined by heating, whereas the destruction of the sample before its melting is determined the formation of a network of microcracks (see [31]).

Manifestations of nonlinearity have been observed for the first time in the synchronous detection widely used in laser experiments. Previous works on this important subject involved the linear acoustic approximation.

Our approach with increasing energy in synchronous detection experiments points to a way to the development of combined methods for the measurement of optical properties in a wide energy range. Synchronous detection (multipulse actions) applied at low energies is continuously transformed to single measurements [29, 35] at high energies of the laser pulse.

ACKNOWLEDGMENTS

Experiments were carried out using the Shared Access Center "Laser Femtosecond Complex," Joint Institute for High Temperatures, Russian Academy of Sciences.

FUNDING

This work was supported by the Ministry of Science and Higher Education of the Russian Federation (agreement no. 075-00270-24-00 with the Joint Institute for High Temperatures, Russian Academy of Sciences, experiments, and state assignment no. FFWR-2024-0013 for the Landau Institute for Theoretical Physics, Russian Academy of Sciences, calculations).

CONFLICT OF INTEREST

The authors of this work declare that they have no conflicts of interest.

REFERENCES

1. C. A. Paddock and G. L. Eesley, J. Appl. Phys. **60**, 285 (1986).
2. C. Thomsen, H. T. Grahn, H. J. Maris, and J. Tauc, Phys. Rev. B **34**, 4129 (1986).
3. S.-S. Wellershoff, J. Hohlfeld, J. Guedde, and E. Matthias, Appl. Phys. A **69** (Suppl. 1), S99 (1999).
4. N. Del Fatti, C. Voisin, M. Achermann, S. Tzortzakis, D. Christofilos, and F. Vallyu, Phys. Rev. B **61**, 16956 (2000).
5. A. A. Mel'nikov, O. V. Misochko, and S. V. Chekalin, JETP Lett. **89**, 129 (2009).
6. I. Razdolski, D. Makarov, O. G. Schmidt, A. Kirilyuk, T. Rasing, and V. V. Temnov, ACS Photon. **3**, 179 (2016).
7. O. Matsuda, M. C. Larciprete, R. Li Voti, and O. B. Wright, Ultrasonics **56**, 3 (2015).
8. C. Thomsen, J. Strait, Z. Vardeny, H. J. Maris, J. Tauc, and J. J. Hauser, Phys. Rev. Lett. **53**, 989 (1984).
9. S. Edward, H. Zhang, I. Setija, V. Verrina, A. Antoncecchi, S. Witte, and P. Planken, Phys. Rev. Appl. **14**, 014015 (2020).
10. H. Zhang, A. Antoncecchi, S. Edward, I. Setija, P. Planken, and S. Witte, Phys. Rev. Appl. **13**, 014010 (2020).
11. C. Thomsen, H. T. Grahn, H. J. Maris, and J. Tauc, Opt. Commun. **60**, 55 (1986).
12. V. E. Gusev and P. Ruello, Appl. Phys. Rev. **5**, 031101 (2018).
13. A. Devos and R. Côte, Phys. Rev. B **70**, 125208 (2004).
14. J. D. G. Greener, E. de Lima Savi, A. V. Akimov, S. Raetz, Z. Kudrynskyi, Z. D. Kovalyuk, N. Chigarev, A. Kent, A. Patané, and V. Gusev, ACS Nano **13**, 11530 (2019).
15. L. M. Barker and R. E. Hollenbach, J. Appl. Phys. **43**, 4669 (1972).
16. G. I. Kanel, S. V. Razorenov, and V. E. Fortov, *Shock-Wave Phenomena and the Properties of Condensed Matter* (Springer, New York, 2004).
17. E. B. Zaretsky and G. I. Kanel, J. Appl. Phys. **110**, 073502 (2011).
18. P. Tengdin, W. You, C. Chen, X. Shi, D. Zusin, Y. Zhang, C. Gentry, A. Blonsky, M. Keller, P. M. Oppeneer, H. C. Kapteyn, Zh. Tao, and M. M. Murnane. Sci. Adv. **4**, 1 (2018).
19. V. V. Temnov, I. Razdolski, T. Pezeril, D. Makarov, D. Seletskiy, A. Melnikov, and K. A. Nelson, J. Opt. **18**, 093002 (2016).
20. J. M. Klopf A. P. Caffrey, P. E. Hopkins, and P. M. Norris, Microscale Thermophys. Eng. **9**, 365 (2005).
21. P. E. Hopkins, J. M. Klopf, and P. M. Norris, Appl. Opt. **46**, 2076 (2007).
22. S. I. Ashitkov, N. A. Inogamov, P. S. Komarov, Yu. V. Petrov, S. A. Romashevskiy, D. S. Sitnikov, E. V. Struleva, and V. A. Khokhlov, High Temp. **60**, 192 (2022).
23. N. A. Inogamov, V. A. Khokhlov, S. A. Romashevskiy, Yu. V. Petrov, V. V. Zhakhovsky, and S. I. Ashitkov, JETP Lett. **117**, 104 (2023).
24. N. A. Inogamov, V. A. Khokhlov, S. A. Romashevskii, A. V. Petrov, M. A. Ovchinnikov, and S. I. Ashitkov, J. Exp. Theor. Phys. **138** (2) (2024, in press).
25. N. A. Inogamov, V. V. Zhakhovsky, S. I. Ashitkov, V. A. Khokhlov, V. V. Shepelev, P. S. Komarov, A. V. Ovchinnikov, D. S. Sitnikov, Yu. V. Petrov, M. B. Agranat, S. I. Anisimov, and V. E. Fortov, Contrib. Plasma Phys. **51**, 367 (2011).
26. D. P. Blair and P. H. Sydenham, J. Phys. E **8**, 621 (1975).
27. M. A. Ordal, R. J. Bell, R. W. Alexander, L. L. Long, and M. R. Querry, Appl. Opt. **26**, 744 (1987).
28. V. E. Gusev and A. A. Karabutov, *Laser Optoacoustics* (AIP Press, New York, 1993).
29. N. A. Inogamov, V. V. Zhakhovskii, S. I. Ashitkov, Yu. V. Petrov, M. B. Agranat, S. I. Anisimov, K. Nishihara, and V. E. Fortov, J. Exp. Theor. Phys. **107**, 1 (2008).

30. H. Kempf, P. Sulzer, A. Liehl, A. Leitenstorfer, and R. Tenne, Commun Phys. **6**, 145 (2023).
31. F. Akhmetov, I. Milov, S. Semin, F. Formisano, N. Medvedev, J. M. Sturm, V. V. Zhakhovsky, I. A. Makhotkin, A. Kimel, and M. Ackermann, Vacuum **212**, 112045 (2023).
32. Yu. V. Petrov and N. A. Inogamov, JETP Lett. **98**, 278 (2013).
33. N. A. Inogamov, Yu. V. Petrov, S. I. Anisimov, A. M. Oparin, N. V. Shaposhnikov, D. von der Linde, and J. Meyer-ter Vehn, JETP Lett. **69**, 310 (1999).
34. S. I. Anisimov, N. A. Inogamov, and A. M. Oparin, Izv. Akad. Nauk, Mekh. Zhidk. Gaza, No. 6, 149 (1999).
35. S. I. Ashitkov, M. B. Agranat, G. I. Kanel', P. S. Komarov, and V. E. Fortov, JETP Lett. **92**, 516 (2010).
36. V. V. Zhakhovskii and N. A. Inogamov, JETP Lett. **92**, 521 (2010).
37. X. W. Wang, A. A. Kuchmizhak, X. Li, S. Juodkazis, O. B. Vitrik, Yu. N. Kulchin, V. V. Zhakhovsky, P. A. Danilov, A. A. Ionin, S. I. Kudryashov, A. A. Rudenko, and N. A. Inogamov, Phys. Rev. Appl. **8**, 044016 (2017).
38. S. A. Romashevskiy, V. A. Khokhlov, S. I. Ashitkov, V. V. Zhakhovsky, N. A. Inogamov, P. S. Komarov, A. N. Parshikov, Yu. V. Petrov, E. V. Struleva, and P. A. Tsygankov, JETP Lett. **113**, 308 (2021).
39. A. A. Ionin, S. I. Kudryashov, L. V. Seleznev, and D. V. Sinitsyn, JETP Lett. **94**, 753 (2012).
40. V. V. Zhakhovskii, K. Nishihara, S. I. Anisimov, and N. A. Inogamov, JETP Lett. **71**, 167 (2000).
41. A. A. Ionin, S. I. Kudryashov, L. V. Seleznev, D. V. Sinitsyn, V. N. Lednev, and S. M. Pershin, J. Exp. Theor. Phys. **121**, 737 (2015).
42. A. A. Ionin and S. I. Kudryashov, JETP Lett. **104**, 573 (2016).
43. S. I. Kudryashov and A. A. Ionin, Int. J. Heat Mass Transf. **99**, 383 (2016).
44. V. V. Shepelev, Yu. V. Petrov, N. A. Inogamov, V. V. Zhakhovsky, E. A. Perov, and S. V. Fortova, Opt. Laser Technol. **152**, 108100 (2022).
45. S. I. Anisimov, V. V. Zhakhovsky, N. A. Inogamov, K. P. Migdal, Yu. V. Petrov, and V. A. Khokhlov, J. Exp. Theor. Phys. **129**, 757 (2019).

Translated by R. Tyapaev

SPELL: OK